nature nanotechnology

Article https://doi.org/10.1038/s41565-024-01674-6

Topological valley Hall polariton condensation

Received: 26 October 2023

Accepted: 10 April 2024

Published online: 24 May 2024

Check for updates

Kai Peng[1,2,3,9], Wei Li[1,3,9], Meng Sun[4,9], Jose D. H. Rivero[5,6], Chaoyang Ti[7], Xu Han[7], Li Ge[5,6], Lan Yang[8], Xiang Zhang[2] & Wei Bao[1,3]

A photonic topological insulator features robust directional propagation and immunity to defect perturbations of the edge/surface state. Exciton-polaritons, that is, the hybrid quasiparticles of excitons and photons in semiconductor microcavities, have been proposed as a tunable nonlinear platform for emulating topological phenomena. However, mainly due to excitonic material limitations, experimental observations so far have not been able to enter the nonlinear condensation regime or only show localized condensation in one dimension. Here we show a topological propagating edge state with polariton condensation at room temperature and without any external magnetic field. We overcome material limitations by using excitonic $CsPbCl_3$ halide perovskites with a valley Hall lattice design. The polariton lattice features a large bandgap of 18.8 meV and exhibits strong nonlinear polariton condensation with clear long-range spatial coherence across the critical pumping density. The geometric parameters and material composition of our nonlinear many-body photonic system platform can in principle be tailored to study topological phenomena of other interquasiparticle interactions.

Topological insulators, initially introduced in the two-dimensional (2D) electron gas system under a magnetic field[1], elucidate a remarkable material state: insulating in the bulk but conducting on the edge[2]. These edges are formed at the interfaces where spatial areas with different topological invariants meet. The fundamental principle of topological invariance protects the unimpeded flow of electrons along the edges without dissipation and backscattering by non-magnetic impurities and disorders. This visionary concept has been adopted for other systems, such as cold atoms[3], acoustics[4,5] and photonics[6–10], and has led to many groundbreaking insights into topological physics.

Recently, cavity exciton-polaritons, due to their part-light part-matter nature, were theoretically proposed to be a distinct nonlinear system with tunable quasiparticle composition and interparticle interactions as a powerful platform to emulate the topological phenomena[11–14]. In a semiconductor microcavity, exciton-polaritons are formed in the strong-coupling regime, where the coupling rate between exciton and cavity photon is much faster than each dissipation rate. These bosonic exciton-polaritons carry small effective mass inherited from their photonic component and strong nonlinearity inherited from their excitonic component, enabling a nonlinear Bose–Einstein condensation process (referred to as polariton condensation) at much elevated temperatures when compared with cold atom systems[15–17]. In contrast to creating lattice potential via laser interference in cold atoms, we can construct almost arbitrary periodic potentials in polariton lattices via nanofabrication, enabling complete band structures and coupling-strength tuning among these atom-like polariton condensates[18,19]. Moreover, in the polariton platform, we can directly visualize the band structures and edge-state propagations in studying

[1]Department of Materials Science and Engineering, Rensselaer Polytechnic Institute, Troy, NY, USA. [2]Nanoscale Science and Engineering Center, University of California, Berkeley, Berkeley, CA, USA. [3]Department of Electrical and Computer Engineering, University of Nebraska–Lincoln, Lincoln, NE, USA. [4]School of Physics and Optoelectronic Engineering, Beijing University of Technology, Beijing, China. [5]Department of Physics and Astronomy, College of Staten Island, CUNY, New York, NY, USA. [6]The Graduate Center, CUNY, New York, NY, USA. [7]Center for Nanoscale Materials, Argonne National Laboratory, Lemont, IL, USA. [8]Department of Electrical and Systems Engineering, Washington University, St Louis, MO, USA. [9]These authors contributed equally: Kai Peng, Wei Li, Meng Sun. e-mail: xiang@berkeley.edu; baow2@rpi.edu

https://doi.org/10.1038/s41565-024-01674-6

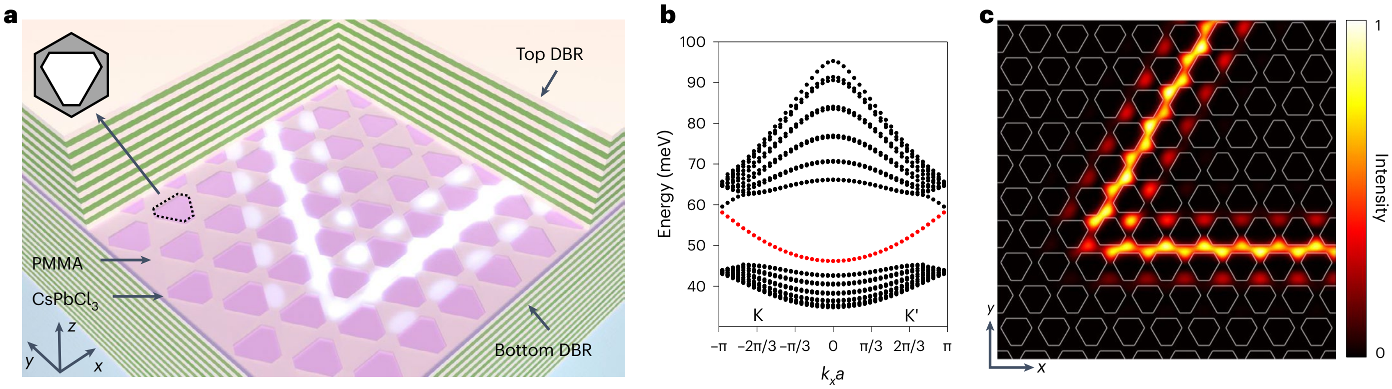

Fig. 1 | Schematics and the design of the polaritonic topological valley edge states. a, Schematic illustration of the perovskite microcavity samples. Our perovskite microcavity consists of a single-crystal $CsPbCl_3$ plate and a patterned PMMA spacer sandwiched between the top and bottom DBRs. Inset: unit cell of the valley Hall crystal. The unit cell consists of a hexagonal hole (EBL-exposed area of PMMA) with two alternating unequal side lengths. By introducing a boundary between domains with opposite hexagonal hole directions, a topological interface with edge states can be formed, as the white highlighted areas shown in **a**. **b**, Projected band structure of the topological interface in a supercell finite in the *y* direction. The topologically protected valley edge states are confined to the interface, as indicated by the filled red circles. The lattice period is $a = 1.2$ µm. **c**, The real-space polariton density distribution of the topologically protected edge state between two spatial lattice areas. The propagating edge state has a continuous distribution even with a sharp corner of 120°. The details of the simulations of **b** and **c** are given in Supplementary Section I.

topological models, which can only be indirectly evidenced in cold atoms. When compared with a pure non-interactive photonic system in the weak-coupling regime, the interactive exciton component of the quasiparticles provides unique tunability of polariton–polariton interactions and opportunities to independently control the exciton and its interactions via external gauge fields[12,13,20,21]. Although efforts with various material platforms have been made to study linear[22–24] and nonlinear[25–27] topological polaritons, they either cannot enter the nonlinear condensation regime or only show localized dot-like condensation in one-dimensional Su–Schrieffer–Heeger models. Thus, a nonlinear polariton platform that can support the most prominent features of topological insulators, such as robust propagating modes against sharp-turn corners or various defects, remains elusive. This restricts the research for developing close analogues of topological condensed matter systems in polariton systems.

Semiconducting lead halide perovskites have recently emerged as a new polaritonic platform at room temperature[28–33], showing excellent performance and offering new opportunities in topological polaritonics. However, due to the in-plane optical birefringence[33,34], polariton lattices with 2D topological interfaces cannot be constructed with the most mature $CsPbBr_3$ materials.

In this work, we overcome these challenges and present the experimental construction of topologically protected propagating modes with polariton condensation. This is achieved by adopting a valley Hall topological insulator lattice and utilizing the isotropic excitonic halide perovskite $CsPbCl_3$ materials. Inspired by the van der Waals valleytronic materials, a valley Hall photonic topological insulator has a valley degree of freedom due to the breaking lattice inversion symmetry and can host topological edge states without an external magnetic field or the construction of photonic pseudospins[35,36]. By integrating topological valley Hall insulator design and high-quality isotropic excitonic halide perovskites, we have fabricated a large and uniform valley Hall polariton lattice and successfully observed topological propagating edge states within a bandgap of 18.8 meV. These edge states exhibit robust transport along the topological interface, encountering sharp turns at the corners of the structures. More importantly, across the critical pumping density, we observed the strong nonlinear polariton condensation of the topologically protected edge states. Interference experiments reveal global phase-locking of the polariton condensates across the entire closed topological interface due to the non-zero polariton in-plane propagation momentum, acting as a coherent topological polariton laser array with low threshold.

Topological polariton valley Hall design and realization

In our experiment, we utilized perovskite $CsPbCl_3$ microcavities, which consist of a large single-crystal $CsPbCl_3$ plate and a polymethyl methacrylate (PMMA) spacer sandwiched between top and bottom distributed Bragg reflectors (DBRs), as shown in Fig. 1a. Previous works based on $CsPbBr_3$ cannot achieve propagating topological edge mode because of the optical birefringence[33,34]. In contrast, the $CsPbCl_3$ crystal has an in-plane isotropic refractive index[29] and was chosen in our experiments to construct the homogeneous potential landscape before the PMMA patterning. We emphasize that this homogeneous landscape is required in most 2D topological propagating edge states (Supplementary Fig. 4). However, due to the low solubility of precursors for Cl-based halide perovskites and the limitation of chemical vapour deposition (CVD) methods, growing large $CsPbCl_3$ thin-film-like single crystals has been quite a challenge. To address this, we carefully modified our growth procedures (see Methods for details) and finally produced thin single-crystalline perovskites with large lateral sizes through either solution synthesis in a nanocavity or CVD. With these crystal samples (Fig. 2a), we then fabricated polariton lattices by patterning the PMMA spacer with standard electron-beam lithography (EBL) on top of the perovskite[31]. A top DBR plate was finally dry-transferred onto the PMMA pattern to form a vertical cavity. Further information on sample fabrication and characterization can be found in Methods and Extended Data Figs. 1 and 2. The typical *Q* factor of the cavity is approximately 400–700 (relatively low, due to the limited reflectivity of the DBR mirror at short wavelength), depending on the thickness and homogeneity of the cavities. The samples show strong coupling between the excitons and the cavity photons with a Rabi splitting of ~280 meV, as shown in Extended Data Fig. 5 for unpatterned samples. The transversely patterned PMMA spacer induced a deep periodic potential of up to ~150 meV, which confines the polaritons in the regions covered by PMMA. The $CsPbCl_3$ also has excellent stability and preserves high optical excitonic quality during the fabrications with treatments such as O_2 plasma and EBL PMMA development in methyl isobutyl ketone/isopropyl alcohol (MIBK/IPA) solution (Extended Data Fig. 3).

The structure of the polaritonic valley Hall insulator is utilized to create topologically protected edge states. Valley Hall insulators break

https://doi.org/10.1038/s41565-024-01674-6

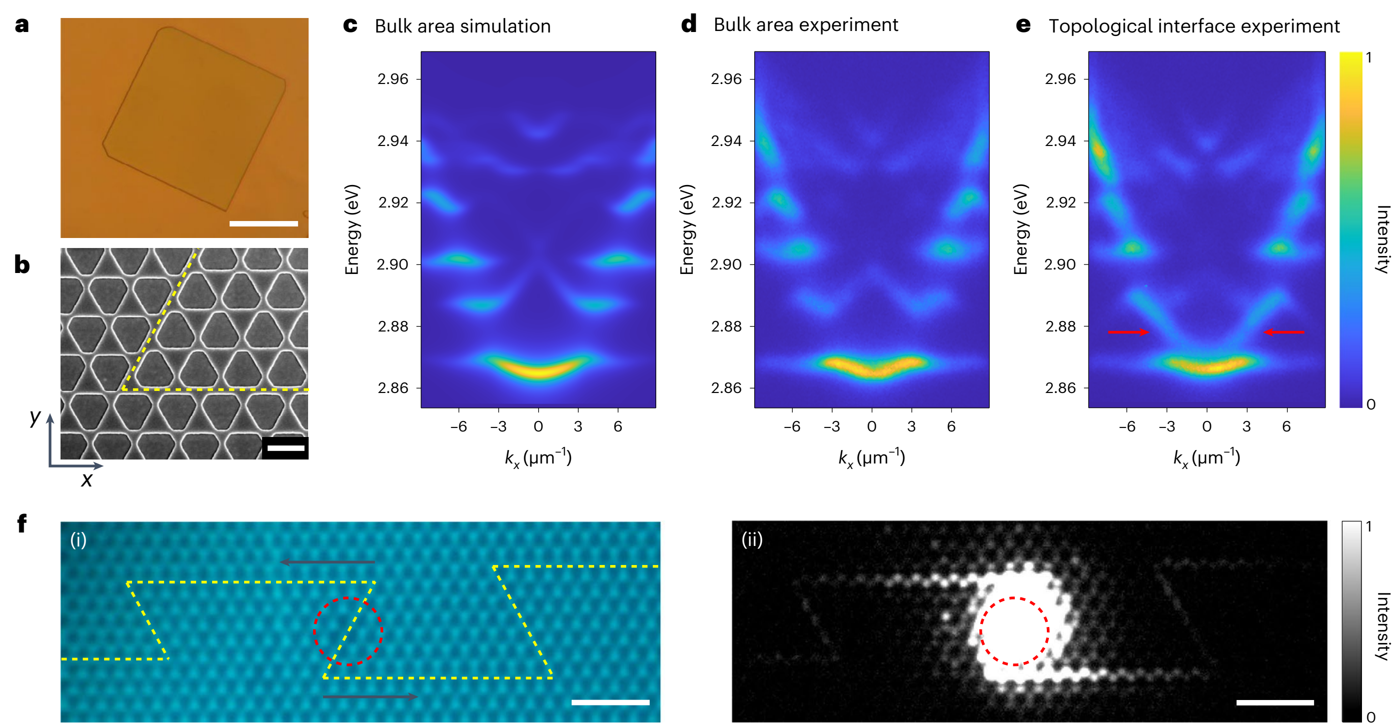

Fig. 2 | Experimental identification of the topological edge states in polariton lattices. a, Optical image of a typical large $CsPbCl_3$ plate transferred onto a bottom DBR substrate. Scale bar: 50 μm. **b**, Scanning electron microscope image of the fabricated sample before transferring the top DBR. A topological interface marked by yellow dashed lines is formed by introducing a boundary between domains with opposite hexagonal hole directions. Scale bar: 1 μm. **c**,**d**, The simulated (**c**) and experimental (**d**) momentum-space dispersions of the bulk area along the *x* axis (K → Γ → K′ direction). A large bandgap of 18.8 meV can be experimentally observed above the ground band in **d**. The dispersion of the bulk area along the *y* axis (ΓM direction) is shown in Extended Data Fig. 6. The dispersions of another sample are shown in Extended Data Fig. 7. **e**, The momentum-space dispersion of the topological interface along the *x* axis. When compared with the bulk area, topological edge states can be clearly observed, as indicated by the red arrows. **f**, Robust propagation of the topological edge states. The real-space image of the waveguide (i) and the saturated PL image of the topological edge state (ii) are shown. The dashed yellow line represents the topological waveguide, and the dashed red circles represent the pumping laser spot. A bandwidth filter (1 nm full-linewidth at half-maximum) is used to filter out the topological edge state (2.881 eV in **e**). The polaritons can clearly propagate across the 120° sharp corner defects, even with a finite polariton lifetime. Scale bar: 5 μm.

the spatial inversion symmetry to achieve valley degrees of freedom without a magnetic field[35,36]. This property has attracted substantial interest in photonics and acoustics to achieve robust waveguide propagation[5,37,38] and electrically pumped terahertz topological lasers at low temperatures[39]. This design has also been theoretically proposed in the interacting bosonic quantum fluids (such as polariton condensates) to achieve topologically protected transport of a chiral vortex[40]. Here, we constructed a lattice structure consisting of hexagonal holes patterned on a PMMA spacer, which breaks the inversion symmetry of the perfect hexagonal holes and leads to the opening of a bandgap at the Dirac points (K and K′) at the corners of the Brillouin zone[35]. This design is more fabrication friendly for EBL patterning and topologically equivalent to the coupled micropillars usually used in the research of polariton lattices, as shown in Supplementary Fig. 3. These gaps have opposite valley Chern numbers of ±1/2, making them topologically distinct (described in Supplementary Section II and Supplementary Figs. 1 and 2). By introducing a boundary between domains with opposite hexagonal hole directions, we created a topological interface with edge states. Numerical simulation (described in Supplementary Section I) shows the edge states (filled red circles) within the bandgap along the interface direction (K → Γ→K′ direction along the *x* axis) in Fig. 1b. Figure 1c shows the real-space polariton distribution of the topologically protected edge state, which reveals that the continuous mode remains robust even with a 120° sharp corner.

Figure 2a displays a typical well-transferred $CsPbCl_3$ plate on a bottom DBR substrate. The large size of the sample enables us to fabricate a uniform 2D polariton lattice with sufficient periods and high excitonic quality. A scanning electron microscope image of a typical sample after EBL patterning is shown in Fig. 2b. The topological interface indicated by yellow dashed lines is formed at the domains where opposite hexagonal hole directions meet. The lattice constant is 1.2 μm, and the short and long sides of the hexagonal holes are 0.27 and 0.73 μm, respectively. In Fig. 2d, the momentum-space (*k*-space) photoluminescence (PL) spectrum of the bulk area along the K → Γ → K′ direction (parallel to the topological interface direction) with non-resonant excitation is presented, and matches well with the simulations shown in Fig. 2c. Notably, a large bandgap of 18.8 meV can be clearly observed above the ground-state band. In contrast, when we excite the interface, an edge band marked by red arrows appears within the bandgap in Fig. 2e, in excellent agreement with the simulations presented in Fig. 1b.

The topological valley Hall effect has shown potential also in photonic waveguides with robust signal transport[37,38]. In our perovskite exciton-polariton system, we explored the polariton propagation along a waveguide structure as illustrated in Fig. 2f. A non-resonant excitation laser spot (indicated by dashed red circles in Fig. 2f) was used in pumping the topological interface. The PL of the edge states was filtered out using a 1 nm bandwidth filter, and the saturated image is shown in Fig. 2f(ii). Clearly, the topological edge states are propagating in two directions along the interface with intrinsic polariton decay, even with three sharp 120° turns, and the small inhomogeneity of the sample does not affect the robustness of their propagation. By comparison, the bulk state diffuses indirectly, and the trivial edge state has substantial loss encountering 120° sharp corners due to the lack of topological protection, as demonstrated in Extended Data Fig. 8.

These different propagations are also proved by the time-dependent numerical simulations (described in Supplementary Section III and Supplementary Videos 1, 2 and 3). These results demonstrate the potential of valley Hall design for the future applications of polaritonic waveguides and switches.

Polariton condensation of valley Hall states

The nonlinear character of the perovskite exciton-polariton enables us to enter the room-temperature polariton condensation regime of the topological edge states, which share closer analogies with topological condensed matter systems. Polaritons are driven–dissipative non-equilibrium systems, allowing them to condense into excited or ground states simply by tuning the gain and loss. To achieve polariton condensation into the topological edge states, we chose an exciton–photon detuning of ~−110 meV to favour polariton relaxation into the edge states. Samples with a closed equilateral triangular boundary of ten periods (along each edge) were fabricated. A 370 nm, 250 fs pulsed laser shaped with a spatial light modulator (SLM) was utilized to pump the triangle's edges non-resonantly. Figure 3d shows the real-space PL emissions of the sample at low pumping power. Here, the triangular topological edges can be clearly identified. A feedback mechanism was employed to adjust the pumping laser profile and facilitate uniform PL emissions of the triangular topological interface (Methods and Extended Data Fig. 4)[41].

Polariton condensation can be observed by performing k-space PL dispersion measurements at increasing pump powers, as displayed in Fig. 3a. Specifically, k-space PL images of the same sample as in Fig. 2d,e are given at 0.05, 0.5, 1 and 1.5 times the condensation threshold pumping power (P_{th}), where P_{th} is approximately 15.2 μJ cm^{-2}. To properly extract the PL emission in these plots only from one of the triangular edges for the polariton dispersion measurements in Fig. 3a, we used a pinhole at the imaging plane to select only the region enclosed by the red dashed circle in Fig. 3d,e (see Extended Data Fig. 4 for details). As the pumping power increases, a clearly nonlinear increase in PL intensity and a narrowing of the linewidth of the edge state can be observed, indicating the occurrence of polariton condensation as shown in Fig. 3b. At 1.5 P_{th}, the system fully condenses at the topological edge states with in-plane momentum along the x axis $k_x = \pm 2.6$ μm^{-1}, as shown in Fig. 3a(iv). Moreover, the real-space image in Fig. 3e unambiguously shows that the condensation occurs only at the triangular interface, providing solid evidence of the topological polariton condensation behaviour of the edge states.

The repulsive interaction of polaritons, which originates from the exciton component, leads to a continuous blueshift of the topological edge mode, a crucial signature of the polariton condensation. Below the condensation threshold, the primary interaction between polaritons and the exciton reservoir causes a stronger blueshift when compared with after the threshold, as demonstrated in Fig. 3c. Noticeably, the blueshift induced by polariton–polariton interactions is more substantial in the topological edge states than in the bulk state due to the spatial selective pumping and the localization of polaritons along the topological edge. As shown in Fig. 3a, the energy gap between the topological edge band (marked as red arrows) and the ground bulk state (marked as orange arrows) at $k_x = 0$ increases with increasing pumping power. To the best of our knowledge, this dynamic tuning of the topological energy band is uniquely associated with the strong-coupling polariton systems. Moreover, it potentially provides a new degree of control for the nonlinear and non-Hermitian topological states[34,42–46].

The non-zero in-plane momentum of the polariton condensates also allows the polariton quantum fluid to flow along the topological interface, which could lead to a global phase-locking of the condensates along the entire edge. To confirm this, we overlapped the real-space image in Fig. 3e with its mirror image using a Michelson interferometer, as shown in Fig. 3f. The interference fringes observed along the entire triangle edge unambiguously justify the long-range spatial phase coherence of the topological condensates. This characteristic also makes the whole topological edges act as a single coherent vertical emitting polariton laser source[47]. In contrast, the condensation of trivial bulk states cannot achieve global phase-locking like that of the topological edge states due to the lack of propagation characteristics, as shown in Extended Data Fig. 10. Our work also presents a larger vertical emitting topological laser array of up to 60 laser emitters (60 triangles on the interface) with a much lower threshold based on a strongly coupled polaritonic system at room temperature, compared with previous studies on topological laser arrays with 30 emitters (30 pillars) using III–V quantum dot weak-coupling photonic systems at low temperatures[48]. Additionally, the use of a standard EBL-patterned PMMA spacer on top of the perovskite layer allowed us to avoid the difficult deep etching of the thick DBR layers in III–V quantum well and quantum dot structures, resulting in better homogeneity in emission profile along the topological edge. Moreover, the spatial coherence of the emitters along the topological edge originates from the in-plane propagation of the topological edge states. Therefore, defects and inhomogeneities, in general, will not compromise coherence build-up along the topological polariton condensation edges, as they typically cannot fully block the in-plane propagation of the modes. This feature was also illustrated in experiments with another sample, as shown in Extended Data Fig. 9.

More samples were fabricated to investigate the condensation coherence of topological edge states in Fig. 4. The condensation of the sample in Fig. 4a exhibits more pronounced interference fringes at zero time delay, indicating better spatial coherent performance. The fringe visibility at zero time delay, that is, $g^{(1)}$ coherence, was extracted in Fig. 4b. Strong spatial coherence along the whole topological interface of the triangle is clearly observed, suggesting global phase-locking. Furthermore, the temporal coherence was also measured by tuning the delay time. The interference fringe amplitude weakens with the increase of delay time, as shown in Fig. 4a. The extracted maximum $g^{(1)}$ is shown in Fig. 4c. The spatial and temporal coherence proves the condensation of the whole topological edge states in our perovskite microcavity.

This topologically protected valley Hall insulator configuration can also be extended to more intricate geometries with multiple sharp corners. To illustrate this, we fabricated two additional topological edge geometries resembling fish with open and closed mouths, as shown in Fig. 5. Remarkably, once the condensation threshold is surpassed, the systems exhibit a uniform condensation at the topological interfaces, as demonstrated clearly in Fig. 5b,d. These compelling results underscore the versatility of our platform, allowing for the investigation of topological phenomena and the utilization of topological polariton laser arrays across a broad spectrum of geometries[49,50].

Conclusions

We have reported the polariton condensation of the topologically protected propagating edge states. This work establishes a room-temperature polariton platform capable of constructing large-scale condensation lattices with arbitrary potential landscapes for emulating topological physics and exploring potential new phases of quantum matter, which were previously inaccessible with low-temperature GaAs and 2D van der Waals material systems. It is worth noting that previous works with topological Chern insulators based on 2D GaAs at low temperatures offer strong topological resilience to defects and disorder theoretically, but require a strong magnetic field to break time-reversal symmetry and open a tiny topological bandgap of only ~0.1 meV (ref. 26) that cannot support condensation at the topological edge state, due to the polariton linewidth (~0.1–0.5 meV) and polariton blueshift (~1 meV). Consequently, only a trivial bulk state condensation outside the bandgap could be achieved. In contrast, valley Hall design lacks broken time-reversal symmetry

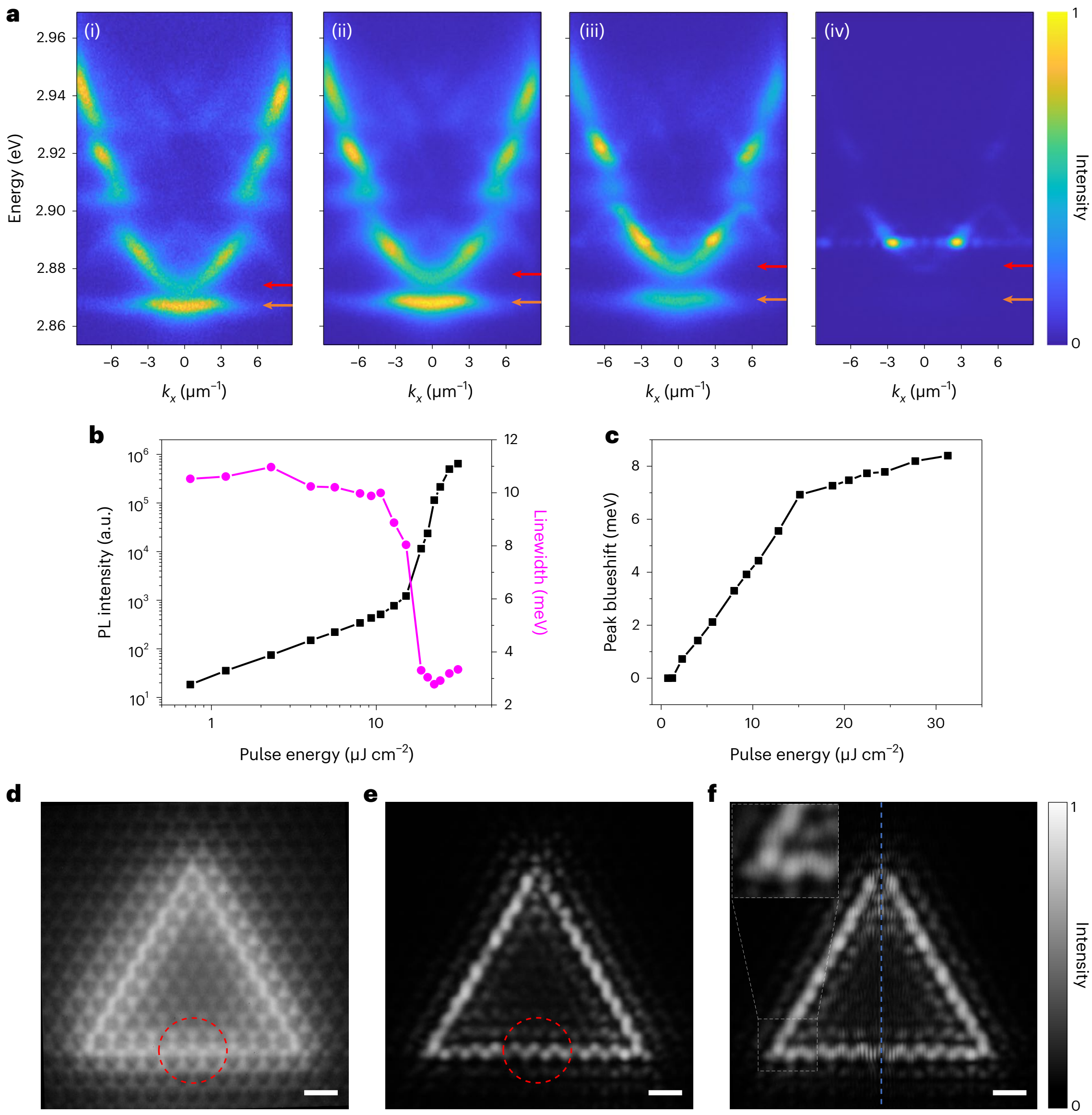

Fig. 3 | Room-temperature polariton condensation of the topological edge states. a, Normalized momentum-space power-dependent PL dispersions of the topological interface along the *x* axis at 0.05 P_{th}, 0.5 P_{th}, P_{th} and 1.5 P_{th} (from left to right, panels (i)–(iv), respectively). P_{th} (~15.2 μJ cm^{-2}) is the pumping fluence of the condensation threshold. The same sample as in Fig. 2d,e is used, but with a larger pinhole in the real-space imaging plane, indicated by the dashed red circles in **d**,**e**, to extract the momentum-space PL. This difference leads to a larger inhomogeneity broadening of the PL spectra when compared with Fig. 2d,e. With increasing pumping power, the topological edge states condense. The edge states were selectively pumped, thus exhibiting a stronger blueshift when compared with the bulk ground state. The red and orange arrows represent the energies of the edge state and the bulk ground state at $k_x = 0$, respectively. **b**, Log–log plot of the integrated PL intensity of the edge state at $k_x = 2.6$ μm^{-1} and the full-width at half-maximum versus pulse energy. The nonlinear increase of the PL intensity and the narrowing of the linewidth strongly support the polariton condensation behaviour. a.u., arbitrary units. **c**, PL peak blueshift of the edge state at $k_x = 2.6$ μm^{-1} versus pulse energy. The repulsive interaction of polaritons induces a continuous blueshift of the topological edge mode. Below the condensation threshold, the primary interaction between polaritons and the exciton reservoir causes a stronger blueshift when compared with after the threshold. **d**,**e**, Real-space PL images below (**d**) and above (**e**) the condensation threshold. An SLM created a triangle profile laser beam to pump the topological edge selectively. The area marked with a red dashed circle corresponds to the power-dependent data in **a**–**c** using a pinhole in the real-space imaging plane, as shown in Extended Data Fig. 4. Above the condensation threshold, the system condenses at the topological interface in **e**. **f**, The interference of the real-space condensation image in **e** and its mirror image symmetrically overlapped along the blue dashed line. The interference fringes demonstrate the phase-locking and the long-range spatial coherence of the triangular topological edges. The inset shows a zoomed-in image of the corner. Scale bars in **d**–**f**: 2 μm.

and can only offer topological protection to defects that respect the symmetry of the lattice (120° sharp corners)[51]. Nevertheless, our $CsPbCl_3$ perovskite system at room temperature shows almost arbitrary large-scale potential landscape and a substantial topological bandgap (18.8 meV in our experiment), enabling the condensation to occur precisely at the pure topological 2D edge states. Moreover, our system can also be extended to chiral perovskite[52] or 2D materials[22,53] for helical polaritons and other exciting topological designs[54], such as quantum spin Hall insulators[22,23,55,56], to manipulate the spin and chiral propagating topological condensations. The low condensation threshold of our platform could lead to electrically pumped polariton lasers[57,58] and inversionless coherent topological polariton laser arrays for future technology applications at room temperature. Finally, the driven-dissipation non-equilibrium and interacting quantum fluid characteristics of polaritons also make them suitable for studying non-Hermitian topological physics.

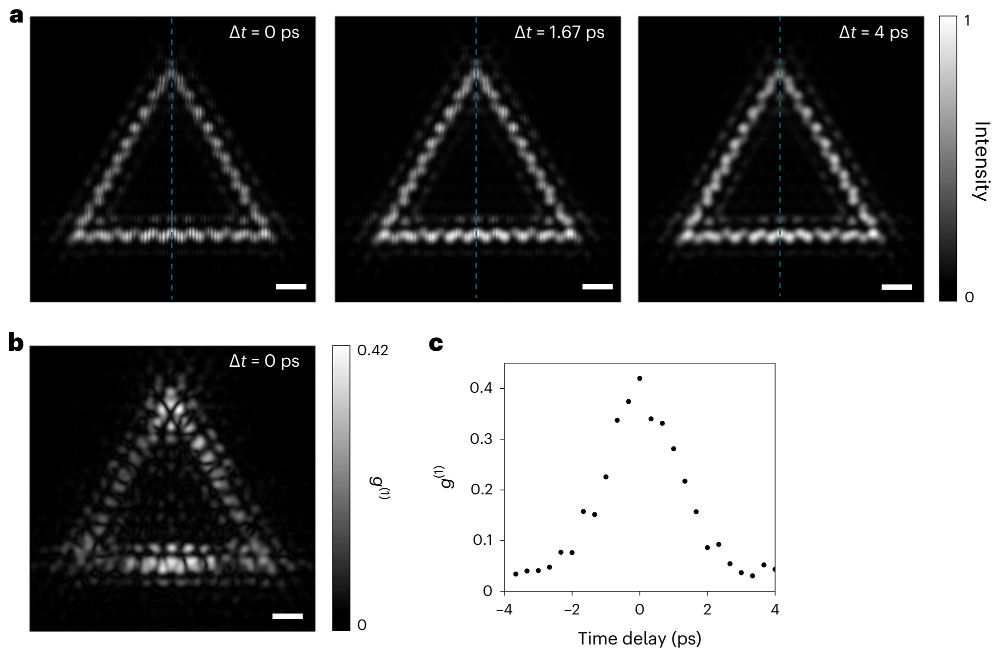

Fig. 4 | Characterization of the spatial and temporal coherence of the topological polariton condensation. a, The real-space interference of the condensation at time delays of 0, 1.67 and 4 ps. The real-space condensation and its mirror images were symmetrically overlapped along the blue dashed line. **b**, The interference visibility (first-order autocorrelation function $g^{(1)}(r, -r)$) of the real-space interference at zero time delay. The interference visibility is obtained from the interferograms using the Fourier transform. Along the triangle topological interface, the condensation shows good coherence. Scale bars in **a**,**b**: 2 µm. **c**, Visibility of interference fringe ($g^{(1)}$) at the centre of the base of the triangle topological interface as a time delay function.

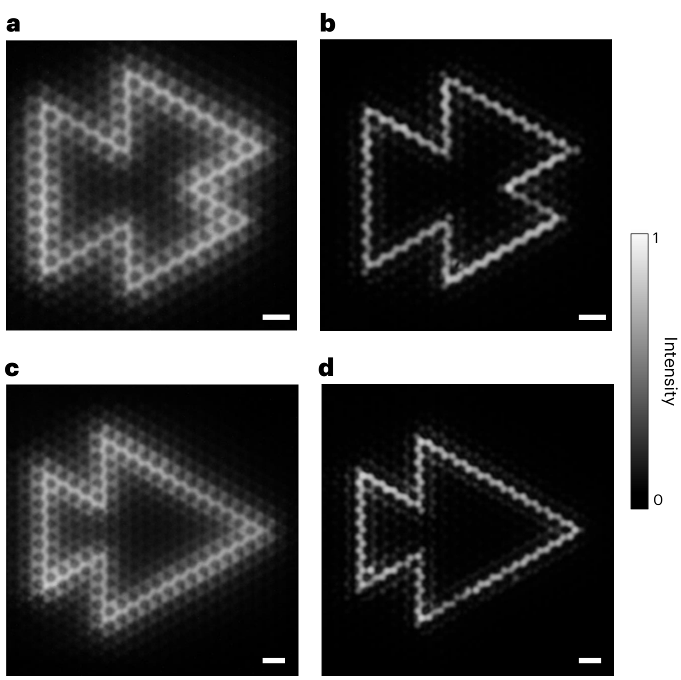

Fig. 5 | Room-temperature polariton condensation of the topological edge states with more complex geometries. a,**b**, Real-space PL images of an 'open-mouth fish' interface below (**a**) and above (**b**) the condensation threshold. **c**,**d**, Real-space PL images of a 'closed-mouth fish' interface below (**c**) and above (**d**) the condensation threshold. Above the threshold, uniform condensations along the topological interfaces can be clearly observed in both cases, proving the potential of our platform to explore the topological phenomena and the applications of topological laser arrays to more intricate geometries. Scale bars: 2 µm.

Online content

Any methods, additional references, Nature Portfolio reporting summaries, source data, extended data, supplementary information, acknowledgements, peer review information; details of author contributions and competing interests; and statements of data and code availability are available at https://doi.org/10.1038/s41565-024-01674-6.

References

1. Klitzing, K. V., Dorda, G. & Pepper, M. New method for high-accuracy determination of the fine-structure constant based on quantized Hall resistance. *Phys. Rev. Lett.* **45**, 494–497 (1980).
2. Hasan, M. Z. & Kane, C. L. *Colloquium*: Topological insulators. *Rev. Mod. Phys.* **82**, 3045–3067 (2010).
3. Cooper, N. R., Dalibard, J. & Spielman, I. B. Topological bands for ultracold atoms. *Rev. Mod. Phys.* **91**, 15005 (2019).
4. Yang, Z. et al. Topological acoustics. *Phys. Rev. Lett.* **114**, 114301 (2015).
5. Lu, J. et al. Observation of topological valley transport of sound in sonic crystals. *Nat. Phys.* **13**, 369–374 (2017).
6. Haldane, F. D. M. & Raghu, S. Possible realization of directional optical waveguides in photonic crystals with broken time-reversal symmetry. *Phys. Rev. Lett.* **100**, 13904 (2008).
7. Wang, Z., Chong, Y., Joannopoulos, J. D. & Soljačić, M. Observation of unidirectional backscattering-immune topological electromagnetic states. *Nature* **461**, 772–775 (2009).
8. Khanikaev, A. B. et al. Photonic topological insulators. *Nat. Mater.* **12**, 233–239 (2013).
9. Lu, L., Joannopoulos, J. D. & Soljačić, M. Topological photonics. *Nat. Photon.* **8**, 821–829 (2014).
10. Ozawa, T. et al. Topological photonics. *Rev. Mod. Phys.* **91**, 15006 (2019).
11. Karzig, T., Bardyn, C.-E., Lindner, N. H. & Refael, G. Topological polaritons. *Phys. Rev. X* **5**, 31001 (2015).

12. Bardyn, C.-E., Karzig, T., Refael, G. & Liew, T. C. H. Topological polaritons and excitons in garden-variety systems. *Phys. Rev. B* **91**, 161413 (2015).
13. Nalitov, A. V., Solnyshkov, D. D. & Malpuech, G. Polariton Z topological insulator. *Phys. Rev. Lett.* **114**, 116401 (2015).
14. Kartashov, Y. V. & Skryabin, D. V. Two-dimensional topological polariton laser. *Phys. Rev. Lett.* **122**, 83902 (2019).
15. Deng, H., Weihs, G., Santori, C., Bloch, J. & Yamamoto, Y. Condensation of semiconductor microcavity exciton polaritons. *Science* **298**, 199–202 (2002).
16. Kasprzak, J. et al. Bose–Einstein condensation of exciton polaritons. *Nature* **443**, 409–414 (2006).
17. Deng, H., Haug, H. & Yamamoto, Y. Exciton–polariton Bose–Einstein condensation. *Rev. Mod. Phys.* **82**, 1489–1537 (2010).
18. Kim, N. Y. et al. Dynamical d-wave condensation of exciton–polaritons in a two-dimensional square-lattice potential. *Nat. Phys.* **7**, 681–686 (2011).
19. Jacqmin, T. et al. Direct observation of Dirac cones and a flatband in a honeycomb lattice for polaritons. *Phys. Rev. Lett.* **112**, 116402 (2014).
20. Cristofolini, P. et al. Coupling quantum tunneling with cavity photons. *Science* **336**, 704–707 (2012).
21. Tsintzos, S. I. et al. Electrical tuning of nonlinearities in exciton–polariton condensates. *Phys. Rev. Lett.* **121**, 37401 (2018).
22. Liu, W. et al. Generation of helical topological exciton–polaritons. *Science* **370**, 600–604 (2020).
23. Li, M. et al. Experimental observation of topological Z2 exciton–polaritons in transition metal dichalcogenide monolayers. *Nat. Commun.* **12**, 4425 (2021).
24. Guddala, S. et al. Topological phonon–polariton funneling in midinfrared metasurfaces. *Science* **374**, 225–227 (2021).
25. St-Jean, P. et al. Lasing in topological edge states of a one-dimensional lattice. *Nat. Photon.* **11**, 651–656 (2017).
26. Klembt, S. et al. Exciton–polariton topological insulator. *Nature* **562**, 552–556 (2018).
27. Dusel, M. et al. Room-temperature topological polariton laser in an organic lattice. *Nano Lett.* **21**, 6398–6405 (2021).
28. Su, R. et al. Perovskite semiconductors for room-temperature exciton-polaritonics. *Nat. Mater.* **20**, 1315–1324 (2021).
29. Su, R. et al. Room-temperature polariton lasing in all-inorganic perovskite nanoplatelets. *Nano Lett.* **17**, 3982–3988 (2017).
30. Peng, K. et al. Room-temperature polariton quantum fluids in halide perovskites. *Nat. Commun.* **13**, 7388 (2022).
31. Su, R. et al. Observation of exciton polariton condensation in a perovskite lattice at room temperature. *Nat. Phys.* **16**, 301–306 (2020).
32. Łempicka-Mirek, K. et al. Electrically tunable Berry curvature and strong light–matter coupling in liquid crystal microcavities with 2D perovskite. *Sci. Adv.* **8**, eabq7533 (2023).
33. Tao, R. et al. Halide perovskites enable polaritonic *XY* spin Hamiltonian at room temperature. *Nat. Mater.* **21**, 761–766 (2022).
34. Rui, S. et al. Direct measurement of a non-Hermitian topological invariant in a hybrid light–matter system. *Sci. Adv.* **7**, eabj8905 (2022).
35. Ma, T. & Shvets, G. All-Si valley-Hall photonic topological insulator. *New J. Phys.* **18**, 025012 (2016).
36. Dong, J.-W., Chen, X.-D., Zhu, H., Wang, Y. & Zhang, X. Valley photonic crystals for control of spin and topology. *Nat. Mater.* **16**, 298–302 (2017).
37. Shalaev, M. I., Walasik, W., Tsukernik, A., Xu, Y. & Litchinitser, N. M. Robust topologically protected transport in photonic crystals at telecommunication wavelengths. *Nat. Nanotechnol.* **14**, 31–34 (2019).
38. He, X.-T. et al. A silicon-on-insulator slab for topological valley transport. *Nat. Commun.* **10**, 872 (2019).
39. Zeng, Y. et al. Electrically pumped topological laser with valley edge modes. *Nature* **578**, 246–250 (2020).
40. Bleu, O., Malpuech, G. & Solnyshkov, D. D. Robust quantum valley Hall effect for vortices in an interacting bosonic quantum fluid. *Nat. Commun.* **9**, 3991 (2018).
41. Töpfer, J. D. et al. Engineering spatial coherence in lattices of polariton condensates. *Optica* **8**, 106–113 (2021).
42. Gao, T. et al. Observation of non-Hermitian degeneracies in a chaotic exciton–polariton billiard. *Nature* **526**, 554–558 (2015).
43. Pernet, N. et al. Gap solitons in a one-dimensional driven–dissipative topological lattice. *Nat. Phys.* **18**, 678–684 (2022).
44. Zhao, H. et al. Non-Hermitian topological light steering. *Science* **365**, 1163–1166 (2019).
45. Solnyshkov, D. D. et al. Microcavity polaritons for topological photonics. *Opt. Mater. Express* **11**, 1119–1142 (2021).
46. Ardizzone, V. et al. Polariton Bose–Einstein condensate from a bound state in the continuum. *Nature* **605**, 447–452 (2022).
47. Kavokin, A. et al. Polariton condensates for classical and quantum computing. *Nat. Rev. Phys.* **4**, 435–451 (2022).
48. Dikopoltsev, A. et al. Topological insulator vertical-cavity laser array. *Science* **373**, 1514–1517 (2021).
49. Bahari, B. et al. Nonreciprocal lasing in topological cavities of arbitrary geometries. *Science* **358**, 636–640 (2017).
50. Bandres, M. A. et al. Topological insulator laser: experiments. *Science* **359**, eaar4005 (2018).
51. Rosiek, C. A. et al. Observation of strong backscattering in valley-Hall photonic topological interface modes. *Nat. Photon.* **17**, 386–392 (2023).
52. Long, G. et al. Chiral-perovskite optoelectronics. *Nat. Rev. Mater.* **5**, 423–439 (2020).
53. Lundt, N. et al. Optical valley Hall effect for highly valley-coherent exciton-polaritons in an atomically thin semiconductor. *Nat. Nanotechnol.* **14**, 770–775 (2019).
54. Berestennikov, A. S. et al. Enhanced photoluminescence of halide perovskite nanocrystals mediated by a higher-order topological metasurface. *J. Phys. Chem. C* **125**, 9884–9890 (2021).
55. Wu, L.-H. & Hu, X. Scheme for achieving a topological photonic crystal by using dielectric material. *Phys. Rev. Lett.* **114**, 223901 (2015).
56. Berestennikov, A. et al. Perovskite microlaser integration with metasurface supporting topological waveguiding. *ACS Nano* **17**, 4445–4452 (2023).
57. Schneider, C. et al. An electrically pumped polariton laser. *Nature* **497**, 348–352 (2013).
58. Suchomel, H. et al. Platform for electrically pumped polariton simulators and topological lasers. *Phys. Rev. Lett.* **121**, 257402 (2018).

Methods

Fabrication of DBR mirror

For the fabrication of the bottom DBR mirror, 100-nm-thick indium tin oxide was first deposited on a quartz wafer to create a charge dissipation layer for EBL, followed by the deposition of 15.5 pairs of SiO_2/Ta_2O_5 by electron-beam evaporation with an advanced plasma source. For the top DBR mirror, 7.5 pairs of SiO_2/Ta_2O_5 were deposited on a silicon wafer with 300 nm PMMA by ion-assisted electron-beam deposition. The top DBR was transferred to a polydimethylsiloxane stamp by dissolving the PMMA. All the DBR and indium tin oxide layers mentioned above have sharp interfaces and ultrahigh flatness.

Synthesis of $CsPbCl_3$ single-crystal microplates

$CsPbCl_3$ single-crystal microplates were grown by solution growth under confinement or CVD. Samples grown using these two methods exhibit similar optical properties.

For solution growth, 0.1 M CsCl and $PbCl_2$ were dissolved in 1 ml DMSO. The supersaturation solution was filtered and dropped at the edge of the bonded 330 nm DBR nanocavity and left for 10 min until the cavity space was fully filled by the solution through capillary force. Due to the poor solubility of CsCl and $PbCl_2$ in DMSO, we modified our previous reported method[34] by placing the cavities in a sealed container filled with toluene vapour to obtain high-quality $CsPbCl_3$ single crystals with large size. The toluene vapour will gradually spread into the precursor solution, leading to an increased local solution concentration, which in turn will promote the initiation of perovskite nucleation. The growth process was kept at 50 °C for 48 h and then put in a vacuum chamber to eliminate any potential leftover solvent. Finally, the after-growth nanocavity with $CsPbCl_3$ microplates was opened for device fabrication.

For the CVD growth, 150-μm-thick high-quality muscovite mica substrates were used in CVD growth. In detail, the growth surface of mica was freshly cleaved and placed face down on the top of a quartz crucible that contained a fine powder mixed with 42 mg CsCl (Sigma-Aldrich; 99.999% purity) and 75 mg $PbCl_2$ (Alfa Aesar; 99.999% purity). The CVD tube was pumped down and fed with N_2 (99.999% purity) three times after the crucible was located in the centre. The tube was maintained at ambient pressure with an N_2 flow rate of 30 sccm. The system was first heated to 575 °C within 30 min, followed by being maintained for 30 min and cooled to 400 °C within 1 h 20 min. After the growth of crystals, the tube was cooled to room temperature naturally.

Fabrication of topological polariton lattice devices

The perovskite plates grown by the solution process can be directly used after opening the bonded cavity. The $CsPbCl_3$ single-crystal microplate grown using CVD was directly transferred from the mica substrate to the bottom DBR using a standard dry-transfer method. A gentle O_2 plasma treatment was used to remove all the residue from the transfer. Then a PMMA spacer layer was spin-coated onto the perovskite microplate, and the topological lattice was patterned via standard EBL with an accelerating voltage of 30 kV, followed by MIBK/IPA 1:3 development for 30 s and IPA rinsing for 15 s, respectively. Finally, the top DBR mirror was transferred on top of the PMMA spacer with the topological pattern using a polydimethylsiloxane stamp. The PL of the perovskite microplate shows no noticeable changes after plasma treatment and development (Extended Data Fig. 3). The thicknesses of the perovskite microplate and the PMMA spacer of the sample in Figs. 2 and 3 were 324 nm and 145 nm, respectively.

Optical measurements of the polariton lattice

The optical measurements of the polariton lattice were performed with a room-temperature home-built transmission set-up, as shown in Extended Data Fig. 4a. A 250 fs optical parametric amplifier pulse laser (370 nm centre wavelength) with a repetition rate of 200 kHz was used to achieve a non-resonant pump. The triangle pumping laser pattern was generated with a HOLOEYE PLUTO reflective liquid-crystal phase-only SLM in a Fourier imaging configuration. The hologram was computed with a Gerchberg–Saxton algorithm and transferred to the pumping objective (Nikon 40× Plan Fluor ELWD, numerical aperture 0.6). The PL was collected using another objective in a transmission configuration. By sampling the PL intensity of the perovskites across the whole triangle pattern from the real-space image by a Princeton electron multiplying charge-coupled device (EMCCD), a feedback method was used to adjust the hologram in the SLM and the uniformity of the triangle pattern[41]. A typical PL image with a triangle pumping pattern is shown in Extended Data Fig. 4b. The momentum-space images were measured using a Fourier imaging configuration with two achromatic tube lenses. An Andor spectrometer equipped with a 2D EMCCD was used to measure the energy-resolved momentum-space dispersions. A pinhole in the real-space imaging plane was used to isolate the PL from other areas. The interference fringe was measured using a CCD camera in a Michelson interferometer.

Data availability

The main data supporting the findings of this study are available within the paper. Extra data are available from the corresponding authors upon reasonable request. Source data are provided with this paper.

Acknowledgements

We thank S. Klembt and T. Cao for discussions and A. Gao from SVOTEK Inc. for assisting with the high-quality DBR mirror coating. W.B. thanks the National Science Foundation for CAREER support (award DMR-2414131) and the Rensselaer Polytechnic Institute for start-up support. W.B., K.P. and W.L. acknowledge support from the Office of Naval Research (awards N00014-21-1-2099 and N00014-22-1-2322) and from Nebraska Public Power District through the Nebraska Center for Energy Sciences Research. X.Z. and K.P. thank the Gordon and Betty Moore Foundation (award 5722) and the Ernest S. Kuh Endowed Chair Professorship for support. J.D.H.R. and L.G. acknowledge funding from the National Science Foundation (award PHY-1847240). Work performed at the Center for Nanoscale Materials, a US Department of Energy Office of Science User Facility, was supported by the US DOE, Office of Basic Energy Sciences, under contract DE-AC02-06CH11357. The research was partly performed in the Nebraska Nanoscale Facility: National Nanotechnology Coordinated Infrastructure and the Nebraska Center for Materials and Nanoscience, supported by the National Science Foundation (award ECCS-2025298) and the Nebraska Research Initiative.

Author contributions

W.B. and K.P. conceived and initiated the project. K.P. performed all optical measurements. W.L. fabricated the microcavity samples with assistance from K.P., C.T. and X.H. W.L. and K.P. grew and characterized the perovskite materials. M.S., J.D.H.R. and L.G. performed all the theoretical analysis and calculations with assistance from K.P. K.P. and W.B. analysed all the data. L.G. suggested the initial design. L.Y. provided valuable insight and suggestions. W.B. and X.Z. supervised the whole project. K.P., W.L., M.S. and W.B. prepared the initial draft of the manuscript. All authors participated in revising the manuscript.

Competing interests

The authors declare no competing interests.

Additional information

Extended data is available for this paper at https://doi.org/10.1038/s41565-024-01674-6.

Supplementary information The online version contains supplementary material available at https://doi.org/10.1038/s41565-024-01674-6.

Correspondence and requests for materials should be addressed to Xiang Zhang or Wei Bao.

Peer review information *Nature Nanotechnology* thanks Alexander B. Khanikaev, Barbara Piętka and the other, anonymous, reviewer(s) for their contribution to the peer review of this work.

 https://doi.org/10.1038/s41565-024-01674-6

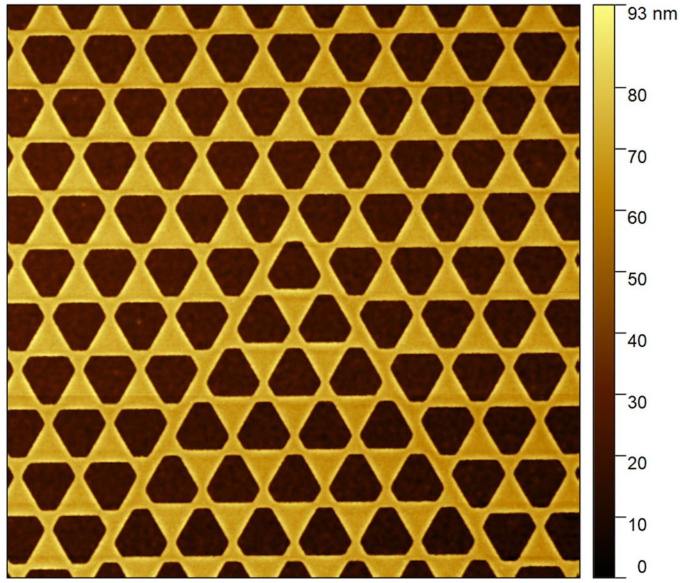

Extended Data Fig. 1 | The AFM image of the patterned PMMA. For this sample, the PMMA spacer has a thickness of ~70 nm. The topological interface can be clearly observed.

https://doi.org/10.1038/s41565-024-01674-6

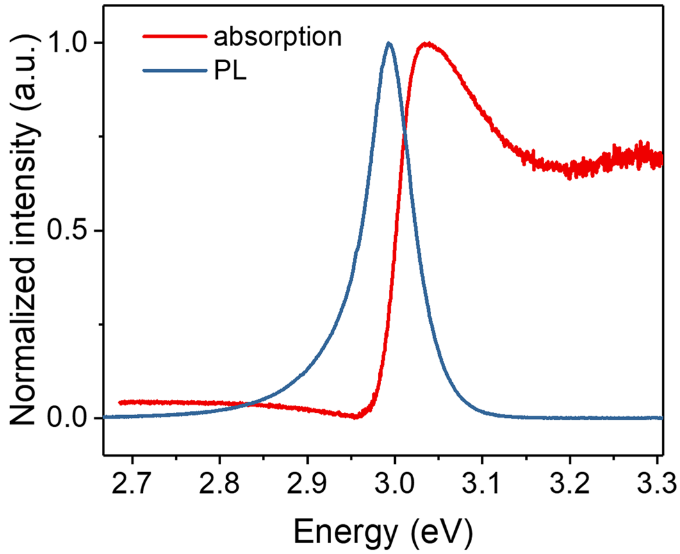

Extended Data Fig. 2 | Room-temperature absorption and PL spectrum of a $CsPbCl_3$ single crystal. The sample shows a strong and stable excitonic absorption peak at room temperature. The corresponding exciton energy peak was extracted as 3.042 eV.

https://doi.org/10.1038/s41565-024-01674-6

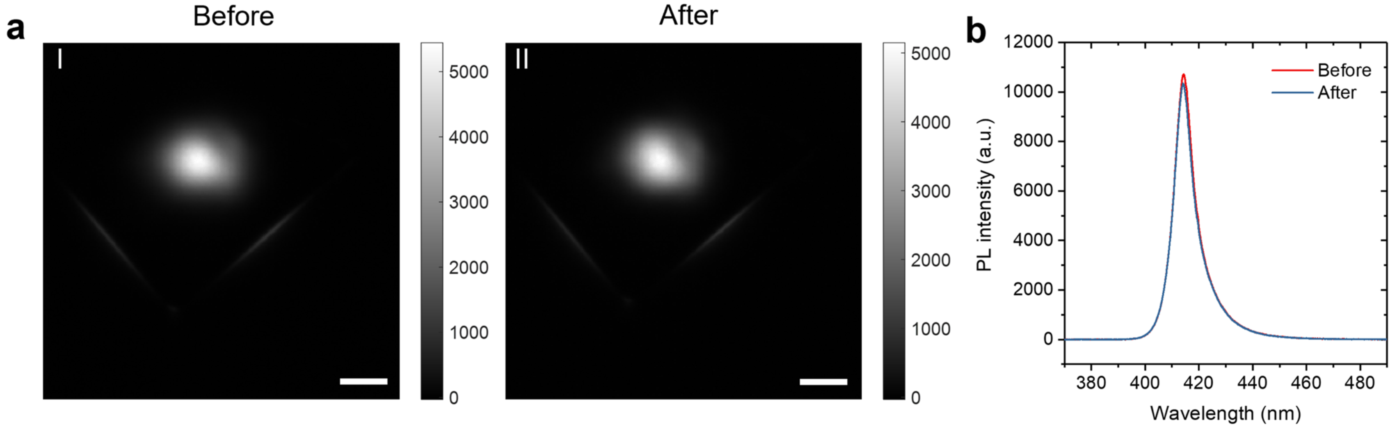

Extended Data Fig. 3 | PL spectra of the $CsPbCl_3$ plate before and after treatments of O_2 plasma and MIBK/IPA developments. a-I-II, The real-space PL images of a single perovskite crystal with non-resonant excitation before and after the treatments of 2 minutes O_2 plasma and 30 s soaking in MIBK/IPA and 15 s rinsing in IPA. **b**, The corresponding PL spectra before and after treatments. Here, after the treatments, the perovskite plate still shows high PL intensity. Scale bars in **a**: 5 µm.

https://doi.org/10.1038/s41565-024-01674-6

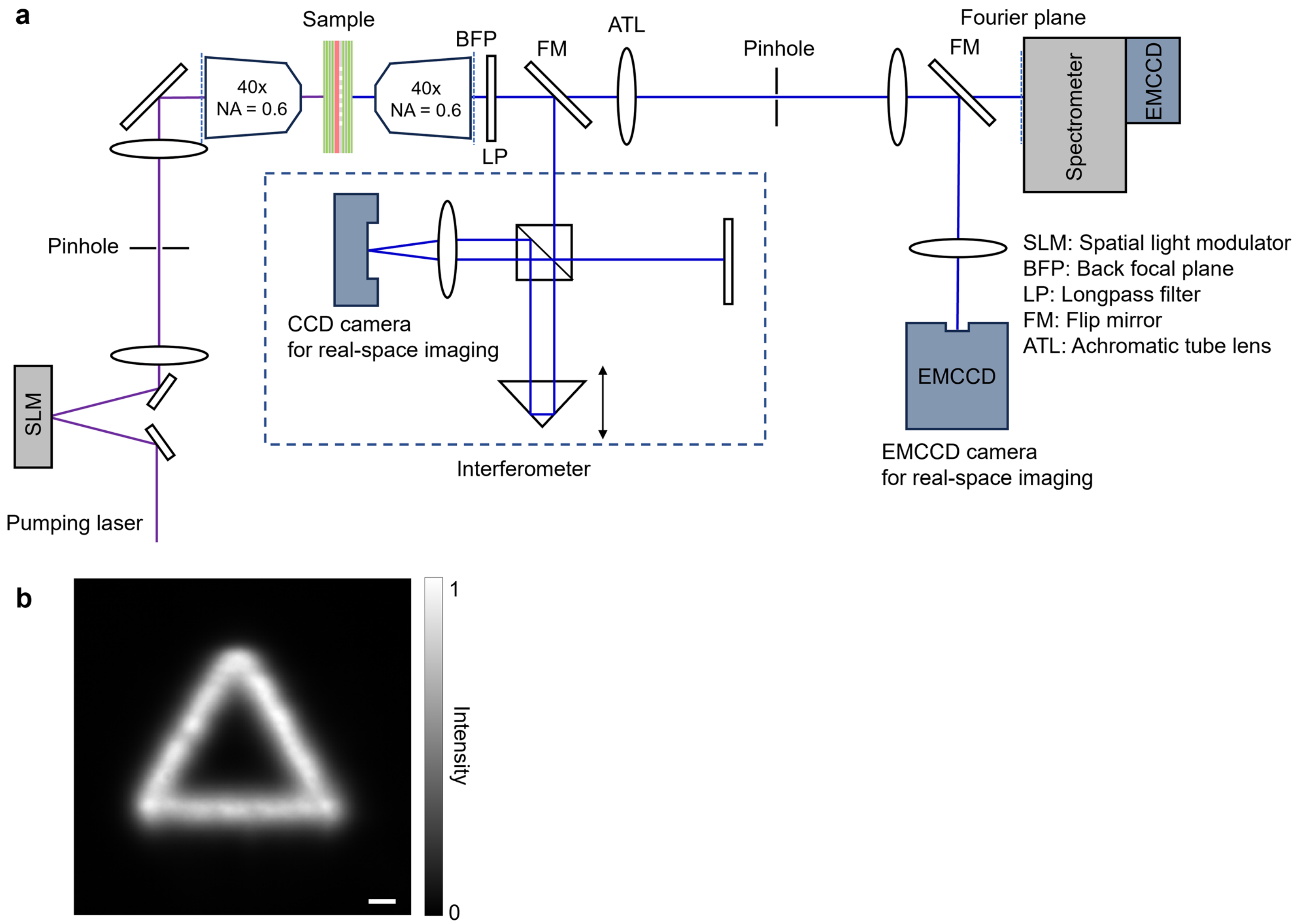

Extended Data Fig. 4 | Diagram of the optical measurement setup. **a**, Experimental setup for the measurement of the polariton lattice at room temperature. A 250-fs pulse laser (370 nm center wavelength) with a repetition rate of 200 kHz was used to achieve non-resonant excitation. A reflective liquid-crystal SLM was used to generate excitation laser patterns in a Fourier imaging configuration. The PL was collected by another objective in a transmission configuration. The momentum-space images can be obtained by a Fourier imaging configuration with two achromatic tube lenses. An Andor spectrometer with a 2D EMCCD was used to measure the energy-resolved momentum-space dispersions. A pinhole at the real-space imaging plane was used to isolate the PL from other areas. A Princeton EMCCD was used to obtain the real-space image. The interference fringe was measured by a CCD camera in a Michelson interferometer. **b**, PL of a bare $CsPbCl_3$ plate with a triangle pattern pumping. By sampling the PL intensity along the triangle pattern from the EMCCD, a feedback method was used to adjust the uniformity of the triangle pattern. Scalebar: 2 μm.

https://doi.org/10.1038/s41565-024-01674-6

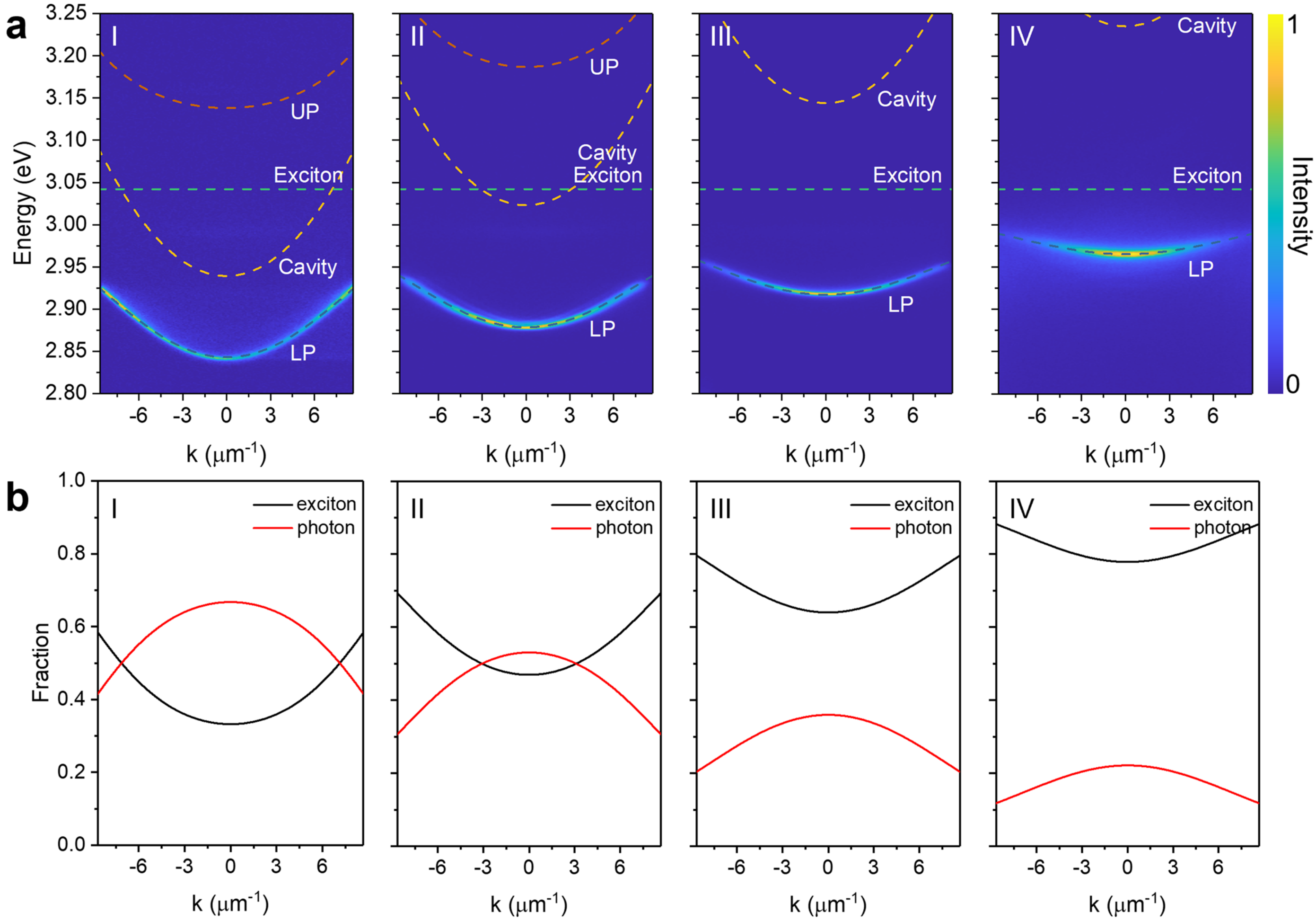

Extended Data Fig. 5 | Characterization of the strong coupling behaviors of unpatterned samples. a-I-IV, Angle-resolved PL dispersions of unpatterned $CsPbCl_3$ microcavities. The dashed lines show the fitting curves based on the coupled model in Supplementary Text Section I. Due to variations in the thickness of different perovskite plates and PMMA coatings, these samples show different strong-coupling behaviors. Here, the exciton energy was extracted from the absorption spectrum in Extended Data Fig. 2 as E_{ex} = 3.042 eV. The cavity effective mass is fitted as m_{cp} = 0.11 meV/(μm/ps)^2 for these four cavities, corresponding to a same refractive index for these perovskites. With detuning change from negative to positive (−103, −19, 97, and 193 meV from I–IV, respectively), the bending effect of the lower polariton branch demonstrates the strong coupling behavior clearly. Due to the strong absorption and large coupling strength, the upper polariton branch cannot be observed. All the lower polariton branches show negligible TE-TM splitting. **b-I-IV**, The corresponding Hopfield coefficients of the lower polariton branches based on the strong coupling model. On the other hand, due to the large Rabi splitting strength, the lower polariton branch can condensate with a large range of fractions of exciton and photon.

 https://doi.org/10.1038/s41565-024-01674-6

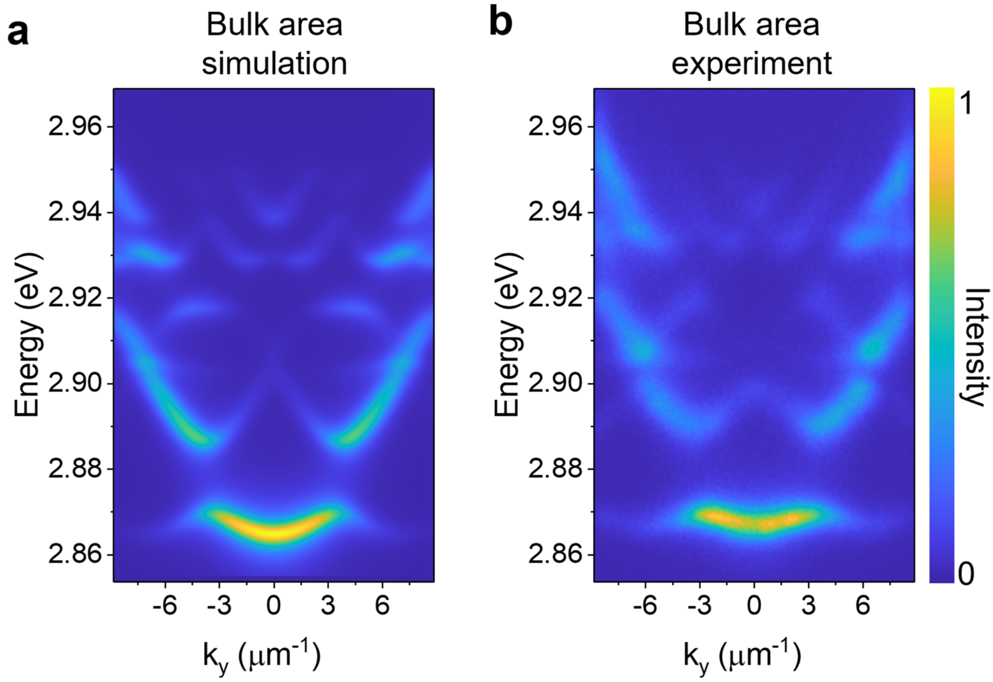

Extended Data Fig. 6 | The momentum-space dispersions along the y-axis. a and **b**, The simulated and experimental momentum-space dispersions of the bulk area along the y-axis (ΓM direction) of the sample in Fig. 2d of the main text, respectctvely.

https://doi.org/10.1038/s41565-024-01674-6

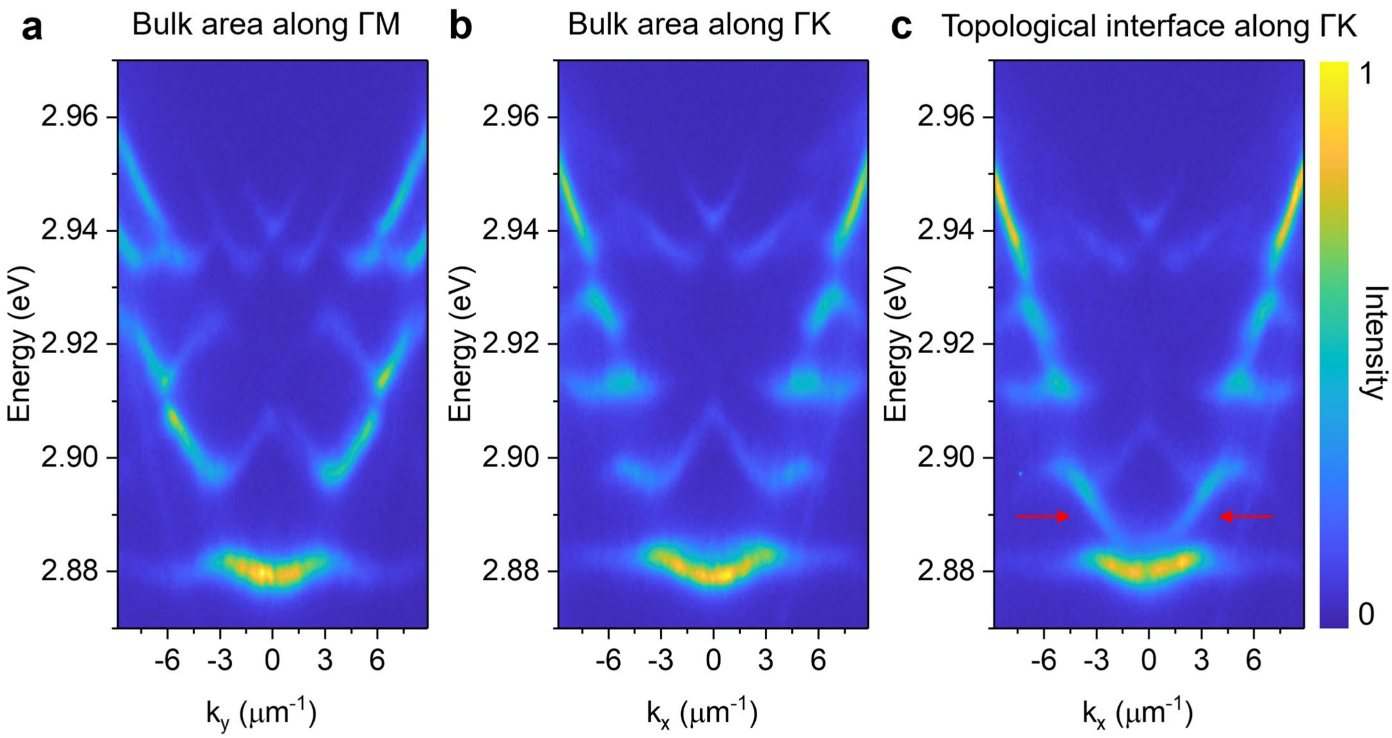

Extended Data Fig. 7 | The momentum-space dispersions of another sample. a and **b**, The PL dispersions of the bulk area along ΓM and ΓK directions, respectively. An energy gap of 14.3 meV was observed in this sample. **c**, The dispersion of the topological interface area along ΓK direction. The topological edge states are observed clearly, as indicated by the red arrows.

https://doi.org/10.1038/s41565-024-01674-6

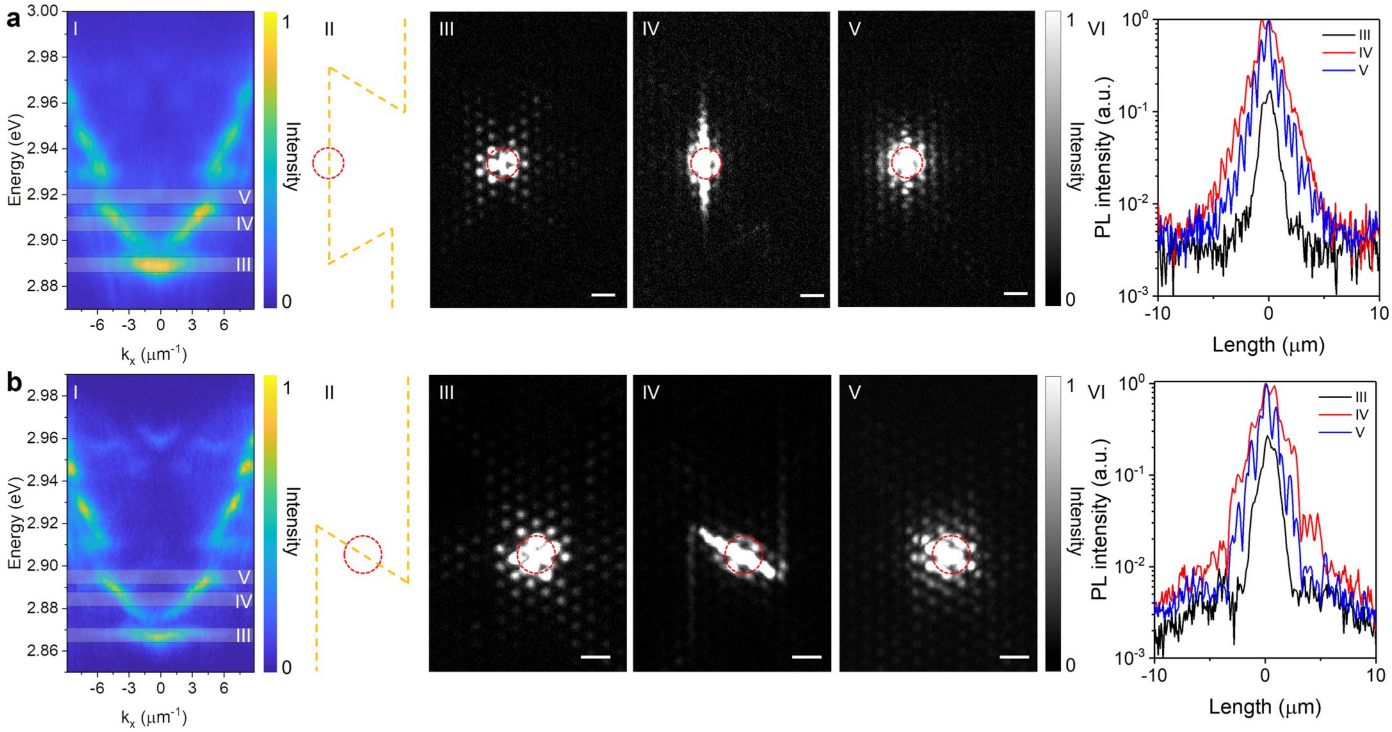

Extended Data Fig. 8 | Energy-resolved polariton propagation of two waveguide samples. a-I, The PL dispersion of the topological interface along the x-axis (K→Γ→K′ direction). A non-resonant laser (dashed red circle) was used to pump the Ω-shaped waveguide, as shown in II. A bandwidth filter (1-nm full linewidth at half maximum) is used to extract polariton PL below, within, and above the topological bandgap, as indicated by the semi-transparent rectangle in a-I. The corresponding saturated real-space propagations are illustrated in the Fig. a-III, a-IV, and a-V, respectively. Only the topological edge state within the topological bandgap in a-IV can propagate along the Ω-shaped waveguides robustly. Comparatively, the bulk state in a-III lacks eigenstates on the interface, leading to undirected diffusion. In a-V, although there are trivial edge states above the topological bandgap, the strong decay occurs when polaritons encounter 120° sharp corners due to the lack of topological protection. This is also illustrated by the normalized PL intensity in a-VI. Due to the maximum PL being in the bulk state in III, the PL intensity on the waveguide is lower than that of the edge states, as shown by the solid black line in Fig. a-VI. There are still some bulk states in a-V because we can only filter the PL signal by a bandwidth filter. It is worth noting that, different from the passive silicon-based waveguides with negligible losses, in our active perovskite microcavity, before polariton condensation, strong absorption from the perovskite gain medium impedes the long-distance propagation of polaritons. A Z-shaped waveguide in another sample also shows similar results in **b**. These different propagations are also proved by the time-dependent numerical simulations (described in Supplementary Text Section III and Supplementary Videos 1–3). These results prove the robust topological propagation of the edge state in our perovskite polariton system. Scale bars in (**a** and **b**): 2 μm.

https://doi.org/10.1038/s41565-024-01674-6

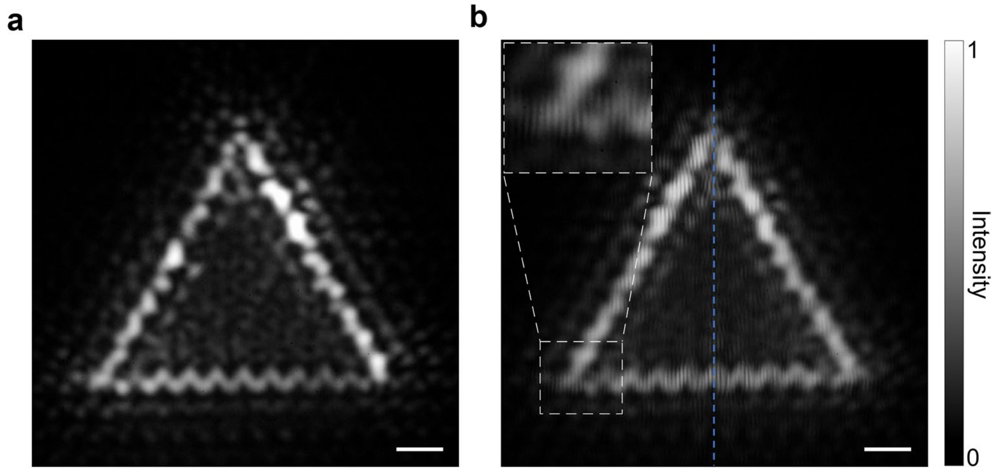

Extended Data Fig. 9 | Another sample for room-temperature polariton condensation of the topological edge states. a, Real-space PL image above the condensation threshold. A triangle laser profile was used to pump the topological edge selectively. Above the condensation threshold, the system condensates at the topological interface. **b**, Interference of the real-space lasing image in **a** and its mirror image. For this sample, even with some defects and clearly noticeable inhomogeneity, the interference fringes still demonstrate the phase-locking and the long-range spatial coherence of the entire triangle topological edge. The inset shows the zoom-in image of the corner. Scale bars in (**a** and **b**): 2 μm.

https://doi.org/10.1038/s41565-024-01674-6

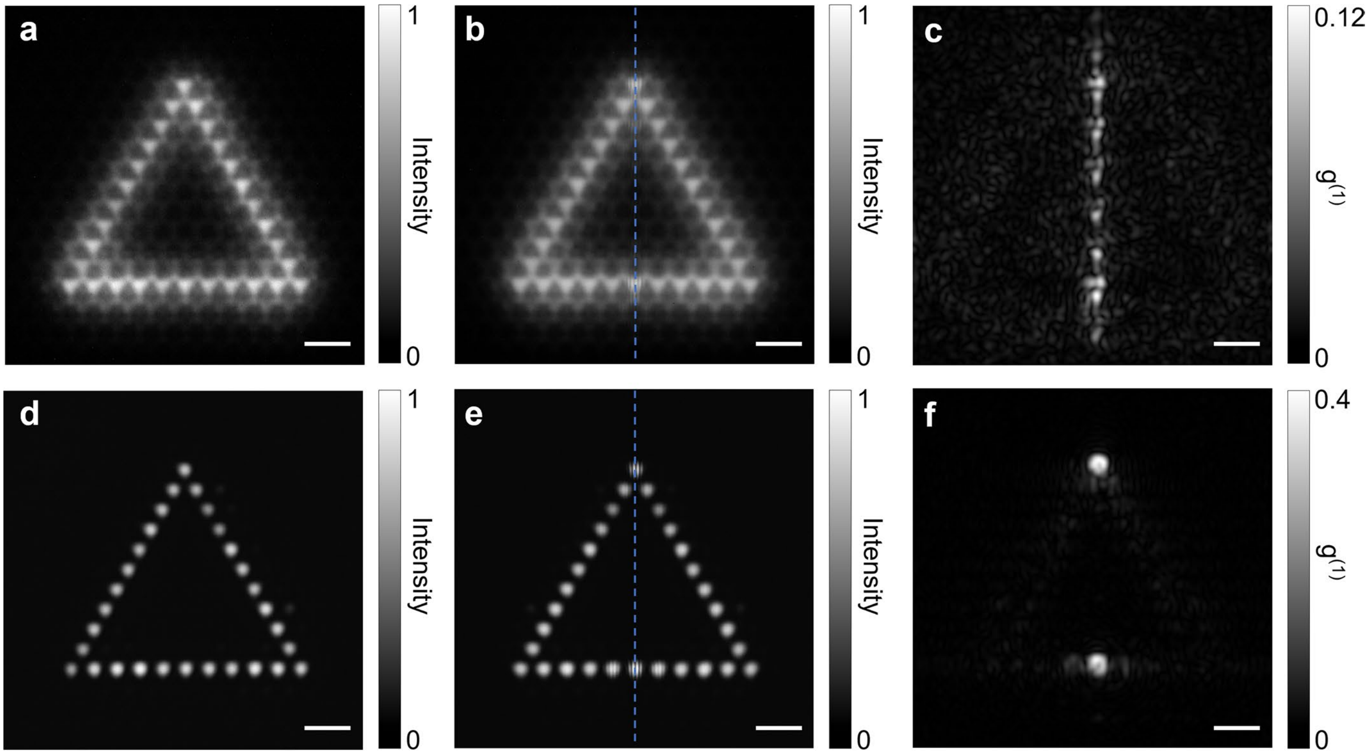

Extended Data Fig. 10 | Room-temperature polariton condensation of the trivial bulk states. a, Real-space PL image below the condensation threshold. A triangle laser profile was used to pump the bulk area. The real-space image and its mirror image were symmetrically overlapped along the blue dashed line. Below the condensation threshold, only short-range interference near the symmetry axis was observed in **b**. **c**, the extracted first-order autocorrelation function $g^{(1)}(r,-r)$ from **b**. **d**, Real-space PL image above the condensation threshold. The condensation occurs at the ground bulk state. Because of the non-propagation character, this bulk condensations act like isolated condensates and no long-range spatial coherence of the entire triangle pumping area was observed in the interference image (**e**) and the extracted interference visibility (**f**). Scale bars in (**a**-**f**): 2 µm.